Spectral entropy and strain energy trends in composite mechanical metamaterials

John T. Klein, Eduard G. Karpov[1]

University of Illinois at Chicago, Department of Civil and Materials Engineering, 842 W Taylor St, Chicago, IL 60607

Abstract

The strain energy and spectral (Shannon) entropy distributions in composite lattices made of core and reinforcement components are investigated by conducting numerical experiments on a set of indefinitely tall lattice strips subjected to a point surface load. The spectral entropy measures the complexity of the strain energy spectrum as it transforms with distance from the loaded surface. The spectral entropy behavior is tailored by adjusting the degree of anisotropy in the lattices. Isotropic continuum-like responses exhibited enhanced spectral entropy decay near the loaded surface and were associated with dispersion of strain energy over a wide spatial area of the lattice. Highly anisotropic responses showed a slow entropy decay at the surface and the localization of strain energy. Interestingly, with sufficient distance from the loaded surface, all lattice designs exhibited the same asymptotic rate of entropy decay, and this rate also was similar to an isotropic continuum material behavior. This implies in practice that any exotic properties of metamaterials determined by their modal selectivity are generally better pronounced in the vicinity of loads, and that they tend to diminish on the periphery of these interesting material systems.

Keywords: mechanical metamaterials, lattice mechanics, Shannon entropy, Parseval energy theorem

1. Introduction

Mechanical metamaterials are artificial structures that exhibit mechanical properties not typically encountered in conventional materials. They are distinguished by an internal architecture, which is a microstructured geometry or topology often consisting of a periodic arrangement of smaller structural building blocks [1–3]. The macroscopic response of the metamaterial is assessed based on an effective medium description without explicitly taking into account internal degrees of freedom, inhomogeneities or other components that exist within the structure. A wide range of mechanical behavior is realized across the different architectures for example, negative effective elastic constants [4–7], multistable structures [8–14], reversal of Saint Venant end effects [10], static non-reciprocity [15, 16] and other behaviors [17, 18].

Recent work in lattice mechanics demonstrated that the internal structure of a material affects the exponential decay of sinusoidal force distributions that are applied statically at the surface and dissipate internally as wavenumber dependent modes of deformation [10, 19, 20]. In these analyses, the static response of the mechanical metamaterial depends on the spatial frequency of the pressure wave, which is analogous to the study of phononic and optical metamaterials where the dynamic response is a function of the frequency of sound and light waves being transmitted [21, 22].

When solving the elasticity equations in the wavenumber domain and performing the inverse Fourier transform to obtain the space domain solution, the displacement field solution to an arbitrary loading state is represented as a superposition of harmonic modes of deformation [20, 23, 24]. In other words, the internal state of deformation of an elastic body can be linearly decomposed into a set of sinusoidal patterns of deformation each with a decay parameter and phase defined based on the internal structure. The amplitudes of the Fourier modes can be determined from the boundary conditions. More recently, it was shown that the strain energy distribution can also be represented in the wavenumber domain as spectral strain energies or strain energy contained in the Fourier modes of deformation [25, 26].

Anisotropy of mechanical metamaterials is expected to play a key role in the complexity of the energy spectrum. Earlier work on highly anisotropic structures showed certain harmonics may decay artificially slowly or be missing due to asymptotic bandgaps [10, 26]. Consequently, the spectral strain energy distribution may be more complex or irregularly shaped at distances away from the loaded surface even though the spatial strain energy may decay fast. Therefore, it is interesting to consider the spectral entropy as a measure of the complexity of the energy spectrum [25],

$$S(X) = -\int_{-\infty}^{\infty} \tilde{w}(X,q) \ln \tilde{w}(X,q) dq \tag{1}$$

where $\tilde{w}$ is strain energy density, q is the wavenumber and X is the material coordinate. The discretized form of the spectral entropy (1) in (8), which will be discussed below, exists on a scale from zero to one. A narrow energy spectrum (pure harmonic as the extreme case) has an entropy value of zero while a broad energy spectrum (flat distribution as the extreme case) has an entropy value of one. Spectral entropy is analogous to Shannon entropy in information theory [27] and, therefore, it can also

Email address: ekarpov@uic.edu (Eduard G. Karpov)
[1]Corresponding author

be interpreted as a measure of how much information is known about the surface load 'signal' as it transmits inside the material. If spectral entropy remains high inside the material then localized traces of the surface load signal persist in the interior. Low spectral entropy occurs when strain energy is distributed uniformly in space, which is the case when details about the surface load signal are not discernible in the interior. Spectral entropy could potentially be used in the information processing of materials deformation, for example, in defect detection. At the position of the defect there would be an increase in entropy due to stress concentrations.

The response of the homogeneous isotropic continuum, described analytically in [25], is the baseline case that will be compared with that of the anisotropic periodic structures in this letter. Spatial and spectral strain energies of the baseline case follow distinct trends, which are in accordance with phenomena such as the Saint Venant principle. In close proximity to the loaded surface, the spatial strain energy density is highly localized with sharp energy gradients or end effects, and the wavenumber domain is characterized by a harmonically rich, broad energy spectrum, i.e., mechanical 'white noise' and maximal spectral entropy that approaches one. Moving along coordinate X into the volume of the material, the spatial strain energy density becomes more evenly distributed with energy gradients disappearing concomitant with end effect decay, and the wavenumber domain is characterized by an energy spectrum that narrows around the zeroth harmonic corresponding to the mechanical 'pure tone' of uniform deformation and spectral entropy that asymptotically approaches zero. As will be shown, the asymptotic behavior of the entropy is similar in metamaterials with very different types of anisotropy, being a major finding of this letter.

2. Composite lattices

The spatial strain energy and spectral entropy behavior is investigated for the two types of composite lattices in Figure 1. Composite lattices are constructed as a combination of a rectangular or triangular lattice 'core', shown in Figures 1a and 1b, respectively, and rhombic lattice 'reinforcement' shown in Figure 1c. By varying the axial rigidity of the core compared to the reinforcement it is possible to control the anisotropy of the structure, which affects the energetic and entropic response. Depending on the choice of core (either rectangular or triangular) and combination of axial rigidities of the core versus the reinforcement, the response of the composite lattices can be tailored to range from isotropic continuum-like behavior to highly anisotropic behavior.

The rectangular lattice is non-rigid and behaves like a folding mechanism while the triangular lattice is a rigid truss meaning deformation is dominated by axial forces, i.e., stretch-dominated [28]. When the reinforcement connections are added to the rectangular and triangular lattices the resulting composite lattices behave as rigid trusses. The composite lattices are highly over-constrained or rigid due to the enhanced number of elastic connections at each node. As will be discussed, the rhombic lattice elements create direct elastic coupling between more distant nodes in space compared to the rectangular or triangular lattice nearest neighbor connections. These more nonlocal connections facilitate dramatic changes in the response compared to the homogeneous continuum as well as the simpler two dimensional lattices.

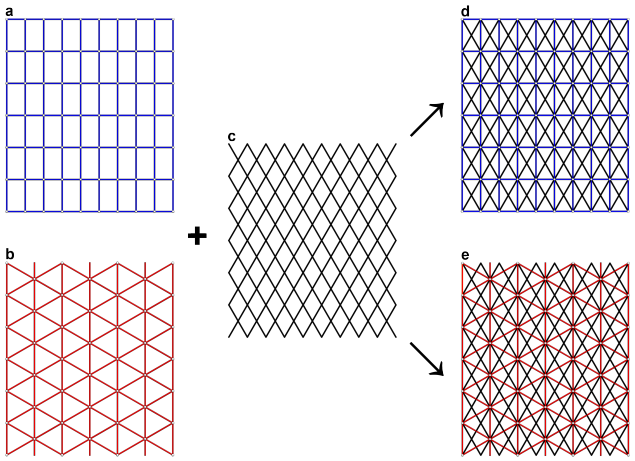

Figure 1: (a) Rectangular and (b) triangular lattices with (c) reinforcing rhombic lattice form the composite lattices in (d,e).

2.1. Unit cell

Unit cells for the composite lattices in Figures 1d and 1e are shown in Figures 2a and 2b, respectively. Unit cell dimensions ensure an identical rhombic reinforcing lattice is overlaid on either type of the core. When constructing the composite lattices with the identical reinforcement, there are 1.5 times as many rectangular unit cells as there are triangular unit cells. The angle α controls the unit cells' aspect ratio. Setting $\alpha = 60^\circ$ produces a lattice of equilateral triangles. In this case, the height H of the rectangular cell is equal to 1.5 times its length L and is equal to the side length of the equilateral triangle.

Primary nodes in the composite lattices are drawn with white circles and correspond to rectangular or triangular nodes. Secondary nodes arise at the self-intersections of reinforcement bars and intersections of reinforcement bars with triangular bars. Performing a balance of momentum at secondary nodes reveals they do not affect displacements at primary nodes and can be neglected in the analysis of rigid lattices. As a result, the reinforcement bars generate a direct elastic coupling between distant primary nodes.

2.2. Axial rigidity ratio

Deformation in a rigid frame is dominated by axial tension and compression in the members. The axial rigidity of a prismatic bar is determined as the product of the area cross section A and Young's modulus E. Numerical experiments in Section 4 will consider anisotropic composite lattices where the axial rigidity of the reinforcing rhombic lattice is distinct from that of the rectangular or triangular core. By varying the relative rigidity between these two components it is possible to control the internal distribution of strain energy and complexity of the energy spectrum as measured by the spectral entropy. The rigidity

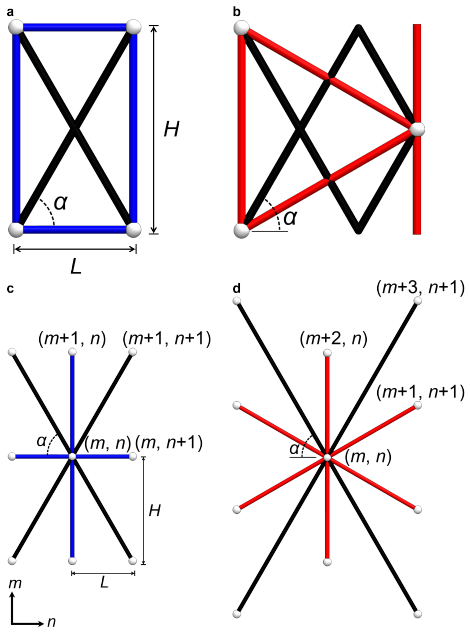

Figure 2: Unit cell representation for (a) rectangular and (b) triangular composite lattices. Associate cell representation for (c) rectangular and (d) triangular composite lattices.

ratio r is the dimensionless design parameter that controls the mechanical response of the lattice, and is written as

$$r = \frac{(EA)_{\text{reinforcement}}}{(EA)_{\text{core}}} \tag{2}$$

Composites lattices with the same ratio r but different absolute values of rigidities are related to each other only by a scale factor. For $r > 1$ the reinforcing rhombic lattice is more rigid compared to the core. Overall, the mechanical response of the composite lattice depends on the choice of the core (triangular versus rectangular) and relative stiffness of the reinforcement versus that of the core (soft reinforcement-stiff core verses stiff reinforcement-soft core).

2.3. Associate cell

The ability of the unit cell to represent all mechanical properties of a lattice falls short especially when more highly nonlocal connections are considered such as the reinforcing rhombus connections [26]. In the field of lattice mechanics, the associate cell is the smallest structural sub unit needed to represent the periodicity and mechanical properties of a lattice, e.g., [23, 29]. Associate cells are shown for the composite lattices in Figures 2a and 2b. For a deeper discussion of the associate cell and its application to exact solutions using the discrete Fourier transform see [10, 19, 20, 26].

The associate cell considers a repeating node indexed at (n, m) and all directly interacting elastic connections to that node. Elastic connections are defined using a set of stiffness matrices or $\mathbf{K}$-blocks, found as submatrices of the stiffness matrix for the entire structure. Equilibrium for the associate cell requires the vector of applied forces $\mathbf{f}_{nm}$ at the current node (n, m) be balanced by the sum of all internal forces arising from the elastic coupling of the current node with all connected nodes (n', m')

$$\mathbf{f}_{nm} = -\sum_{n'}\sum_{m'} \mathbf{K}_{n-n'm-m'}\mathbf{d}_{n'm'} \tag{3}$$

The range of n' and m' depends on the number of elastic connections in the associate cell and how the nodes are indexed. For instance, equilibrium of the rectangular composite associate cell in Figure 2a sums from $n' = n - 1$ to $n + 1$ and $m' = m - 1$ to $m + 1$ for a total of nine terms on the right-hand side. Equilibrium for the triangular composite associate cell in Figure 2b sums from $n' = n - 1$ to $n + 1$ and $m' = m - 3$ to $m + 3$ for a total of eleven terms on the right-hand side. The displacement vector $\mathbf{d}$ at any node can be determined by solving the finite difference equation (3), which can be solved by a range of numerical and semi-analytical techniques, e.g., [10, 19, 20, 23, 26, 29].

2.4. Spatial strain energy

Internal forces on the right-hand side of (3) are premultiplied by the conjugate transpose of the corresponding nodal displacement vector $\mathbf{d}^*_{n'm'}$ and the factor $1/2$ to form a nodal energy term [19, 26, 29]

$$W_{nm} = \frac{1}{2}\sum_{n'}\sum_{m'} \mathbf{d}^*_{n'm'}\mathbf{K}_{n-n'm-m'}\mathbf{d}_{n'm'} \tag{4}$$

W_{nm} is the spatial strain energy discretized at node (n, m). It is a half sum of all strain energies U^e of elements that are directly connected to the node (n, m) in the associate cell, Figure 2. The spatial energy W_{nm} gives the volumetric distribution of strain energy from node to node in discrete lattices and is analogous to the strain energy density in continuum mechanics. For example, performing a finite sum of the spatial strain energy over all nodes in the lattice $\sum_{n,m} W_{nm}$ is like an 'integration' over the volume and is equal to the external work input to the system (10). After solving for W_{nm} at each node, the result is a two dimensional discrete field of nodal energies. A smooth contour plot can be generated by interpolating that discrete field. Strain energy contours will be produced from the numerical experiments in Section 4 and reveal qualitatively how strain energy transforms throughout the lattice interior.

When spatial strain energies are summed over a single index m for a fixed column index n, the following expression for the column energy is defined

$$\Pi_n = \sum_{m} W_{nm} \tag{5}$$

Π_n gives the strain energy in a lattice column formed by all nodes indexed by m. Dependence of this quantity on the column index n reveals whether energy is concentrated at the surface or dispersed throughout the lattice volume. In general, Π_n will decrease monotonically when moving away from the surface of the applied load. However, the parameter r as well as the type of core (rectangular or triangular) will influence how quickly the column energy decays with distance. In the next section, an equivalent representation of Π_n is computed, alternatively by summing spectral energies over the wavenumber. This is the basis of the Parseval energy theorem [25, 26].

3. Strain energy spectral properties

The discrete Fourier transform applied to the vertical index m decomposes the spatial displacement field $\mathbf{d}_{nm}$ into a set of spectral displacements $\tilde{\mathbf{d}}_n(q)$ (A.2) that are functions of the wavenumbers q. There are M wavenumbers q that span the Fourier domain, $[-\pi, \pi]$ where M is the nodal height of the lattice. Each wavenumber is associated with a spatially harmonic loading profile that in turn induces a harmonic response or eigenmode within the structure [20]. The zero eigenmode is a state of uniform deformation associated with a pressure load over a column of nodes. The finest wavelength eigenmode $q = \pi$ occurs when loads of constant magnitude alternate in direction at each subsequent node in the column. By the definition of the inverse DFT, the displacement solution (A.3) to an arbitrary loading state is the superposition of all Fourier modes of deformation. For a deeper discussion of the theory of DFT and its application to lattice mechanics see [10, 19, 20, 23, 26, 29]. In the current investigation, spectral displacements are only required to compute the spectral strain energy and spectral entropy.

3.1. Spectral strain energy

The spectral strain energy $\tilde{W}_n(q)$ (A.12) gives the distribution of strain energy contained in the Fourier modes of deformation at the column n, and is derived from the mechanical Parseval energy theorem in the form of Appendix A suggested by Karpov and coworkers [25, 26]. The Parseval theorem states that the strain energy in the column Π_n, originally expressed as the summation of spatial strain energies over the nodal index m, is equivalently expressed as a summation of the spectral strain energy modes over the wavenumbers q

$$\Pi_n = \sum_m W_{nm} = \frac{1}{M} \sum_q \tilde{W}_n(q), \quad \forall q \in [-\pi, \pi] \tag{6}$$

The column energy Π_n is the sum of spatial strain energies W_{nm} for all nodes in the column. It is interesting to note that the spectral representation of the strain energy $\tilde{W}_n(q)$ is an additive quantity in terms of the superposition of several harmonic loads. In contrast, the usual spatial representation of the strain energy is well known not to be additive.

3.2. Spectral (Shannon) entropy

After obtaining the spectral energy distribution at each column in the lattice it is possible to write the spectral (Shannon) entropy h_n. First, the normalized fractional energy is written

$$p_n(q) = \frac{1}{M} \frac{\tilde{W}_n(q)}{\Pi_n}, \quad \sum_q p_n(q) = 1 \tag{7}$$

where $p_n(q)$ normalizes the energy contained in each wavenumber $\tilde{W}_n(q)$ by the column energy Π_n and the factor $1/M$ such that at any column the summation of all fractional energies is equal to a unit. Then the spectral entropy for discrete lattices is

$$h_n = -\frac{1}{\ln M} \sum_q p_n(q) \ln p_n(q) \tag{8}$$

where $1/\ln M$ is a normalization factor such that h_n ranges from zero to one. The spectral entropy (8) is a measure of spectral complexity of the strain energy in a given position n of the lattice. The rate of decay of the spectral entropy is defined using the first order forward finite difference as

$$\left.\frac{\Delta h_n}{\Delta X}\right|_n = \frac{h_{n+1} - h_n}{\Delta X} \tag{9}$$

where ΔX is the horizontal distance between neighboring nodes n and $n+1$. Spectral entropy decay (9) is the numerical derivative or 'slope' of the spectral entropy h_n (8) at node n with respect to the material coordinate X.

4. Numerical experiment

Triangular and rectangular composite lattices of the types in Figures 1d and 1e are constructed as tall strips where the vertical height along Y is eight times greater than the horizontal width along X in order to mitigate the influence of the horizontal boundaries. Both lattices have $M = 512$ unit cells in the vertical direction. The triangular lattice has $N = 64$ unit cells in the horizontal direction. The rectangular lattice has $N = 96$ unit cells in the horizontal direction whose unit cell is 1.5 times narrower than that of the triangular lattice. As a result, the range of the material coordinate X is from 0 to 96 for both lattices. The contour plots in Figures 3 and 4 show energy distribution in the middle square portions of those tall strips. A point load $\mathbf{F}$ is applied at the middle of the left-hand side at $(0, 0)$ while all other nodes at this end are free of loads or constraints. Right-hand side node have fixed boundary conditions on both degrees of freedom.

The response in a composite lattice strip is controlled by a single design parameter, which is the dimensionless axial rigidity ratio r in (2). This parameter is varied by changing the axial rigidity of the rhombic reinforcement relative to the rectangular or triangular core. In the numerical experiments, the parameter r is first defined for a particular lattice composite strip. Next, the exact values of axial rigidities $(EA)_{\text{scissor}}$ and $(EA)_{\text{core}}$ are chosen so that a unit horizontal force applied at the middle left node $\mathbf{F} = \left(\begin{smallmatrix}1\\0\end{smallmatrix}\right)$ generates a unit horizontal displacement $\mathbf{u} = \left(\begin{smallmatrix}1\\0\end{smallmatrix}\right)$ in the same node. Furthermore, defining axial rigidities such that a unit force causes unit displacement means the external work is the same across all test specimens. The energy balance requires

$$\sum_e U^e = \frac{1}{2} \mathbf{F} \cdot \mathbf{u} = 0.5 \tag{10}$$

Work of the external force $\mathbf{F}$ is converted into stored strain energy as the lattice deforms elastically to accommodate the load. Adding together all element strain energies $\sum_e U^e = 0.5$ is equal to the external work. The constant work of this amount employed in all experiments permits a one-to-one comparison across different lattice designs. Although the total amount of energy input into each lattice strip is constant, how the strain energy is distributed in space and over the wavenumbers will change based on the parameter r as well as the type of lattice (rectangular or triangular).

4.1. Spatial strain energy contours

Spatial (volumetric) strain energy contours, the top three plots in Figures 3 and 4, are produced for three different designs of the rectangular and triangular composite lattices, for a total of six different lattices. Lattices are subjected to the point load as described above. Lattices vary from a very rigid core $r = 0.1$ case to a very rigid reinforcement $r = 100$ case. Results are generated by computing the spatial strain energy W_{nm} by (4) at each node and then creating a color-coded contour that smoothly interpolates the discrete field. To account for the fact that the rectangular lattice has more nodes per unit volume than the triangular lattice, its strain energy contours are normalized by a factor of 1.5.

Starting with the rectangular composite results in Figure 3, the contour for $r = 0.1$, which uses a ten times more rigid rectangular core compared to its reinforcement, shows confinement of strain energy as it focuses along a line in the direction of the applied load. Stiff rectangular bars along this path absorb large amounts of volumetric strain energy compared to the soft reinforcing bars. As will be observed in other designs, the stiffer or more rigid component is responsible for controlling the strain energy distribution. This phenomenon is not obvious from the bar element theory where stiffer bars absorb less strain energy under the force-response curve for a constant applied force. However, this argument does not take into account the nonlocal two dimensional geometry of the problem, which is the main reason for a stiffer component to absorb strain energy in a composite lattice.

The second contour $r = 3.6$ in Figure 3 corresponds to a rectangular lattice design that optimizes spectral entropy decay with distance from the loaded surface. The optimal design r for each type of lattice is defined as the global minimum of the curves in Figure 5, which will be discussed more in the next section. In regards to the contours, increasing the rigidity of the reinforcement promotes the widening or outward deflection of strain energy while increasing the rigidity of the rectangular elements promotes the focusing of energy along the line of applied load. Phenomenologically, the optimized design of these two components produces a response that disperses or redistributes strain energy over a wide spatial region of the lattice. It is interesting to observe that the limit cases of a pure rectangular lattice ($r \to 0$) and rhombus reinforcing lattice ($r \to \infty$) are mechanisms by themselves and thus are unable to disperse strain energy. However, when combined together the response of the composite lattice can be engineered to be continuum-like, i.e., behaves with enhanced strain energy dispersion and spectral entropy decay. Nevertheless, because the structure is inherently discrete with deformation restricted to directions along bar elements, there is still significant outward deflection of strain energy and non-convex contours, effects that are not present in the homogeneous isotropic continuum [26].

The third contour $r = 100$ in Figure 3 has a one hundred times more rigid reinforcement compared to the rectangular core. Similar to the $r = 0.1$ design, the high anisotropy of this design is associated with strain energy localization. However, in this case the strain energy is redirected along angles in

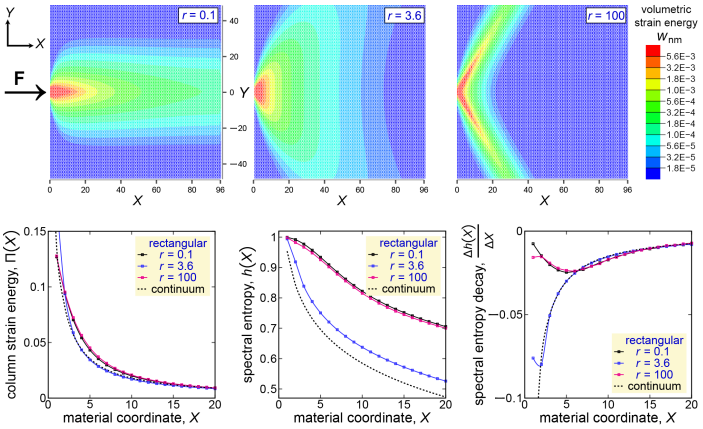

Figure 3: Rectangular lattice behavior; strain energy W_{nm} contours from (4) for design parameters $r = 0.1, 3.6, 100$ using (2) (top); column sum of strain energy $\Pi(X)$ from (5) (bottom left); spectral entropy $h(X)$ from (8) (bottom middle); spectral entropy decay $\Delta h(X)/\Delta X$ from (9) (bottom right).

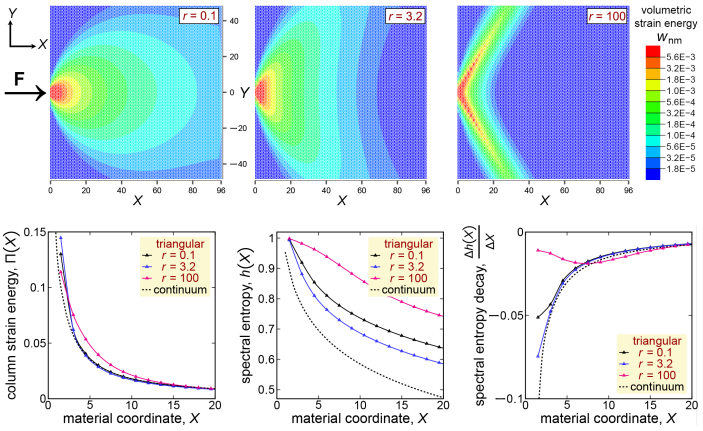

Figure 4: Triangular lattice behavior; strain energy W_{nm} contours from (4) for design parameters $r = 0.1, 3.2, 100$ using (2) (top); column sum of strain energy $\Pi(X)$ from (5) (bottom left); spectral entropy $h(X)$ from (8) (bottom middle); spectral entropy decay $\Delta h(X)/\Delta X$ from (9) (bottom right).

the direction of the reinforcing bars. This deflection of strain energy is explained mathematically on the basis of interference of the Raleigh (decaying Fourier) modes of deformation, see Appendix B. The response is dominated by the rigid reinforcement with minor influence of the soft rectangular core. The soft core helps to spread out the strain energy within the confined paths. In practice, the strain energy deflection effect would still occur if the softer core was another type of lattice such as the triangular lattice of this paper or even a continuous material matrix that fills the space between the rigid reinforcement.

Strain energy contours for the triangular lattice are shown in the top of Figure 4. The biggest difference between the triangular and rectangular contours is the rigid core case $r = 0.1$, which approaches to the strain energy distribution of a pure triangular lattice ($r \to 0$) with some minor influence of the soft reinforcements. Since the triangular core is rigid, this response is continuum-like in the sense that strain energy is dispersive and contours are round and smooth. The middle contour $r = 3.2$ in Figure 4 is the mathematically optimized design for spectral

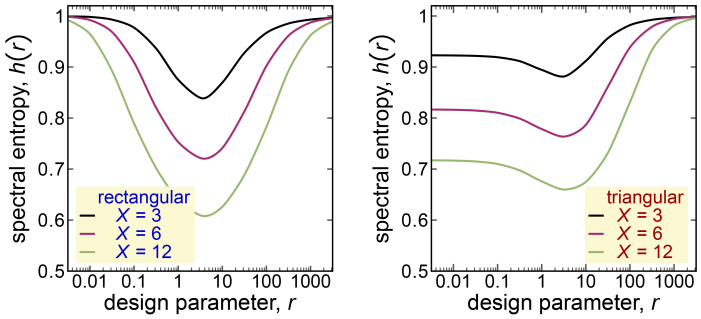

Figure 5: Spectral entropy behavior $h(r)$ as a function of the lattice design parameter r in (2) for the rectangular lattice (left) and triangular lattice (right). Behavior are given for three material coordinates $X = 3, 6, 12$.

entropy decay and shows enhanced strain energy dispersion. Since the triangular core is already dispersive, it is surprising that the most optimal design requires a 3.2 times more rigid reinforcement. The more rigid reinforcement better disperses strain energy vertically and widens contours. Finally, the right contour in Figure 4 is the triangular composite fabricated with a one hundred times more rigid reinforcement relative to the core. Strain energy is localized and deflected along angles of the reinforcement. The result is nearly identical to that of the reinforcement dominated response in the rectangular lattice in Figure 3.

4.2. Column strain energy and spectral entropy plots

Figures 3 and 4 graph the column strain energy (6), spectral entropy (8) and spectral entropy decay (9) dependence on the material coordinate X in the rectangular and triangular lattices. Behavior of the isotropic continuum is plotted for reference, which is an analytical formulation from [25]. In order to overview the behavior across all designs, Figure 5 plots the spectral entropy for each type of lattice but as a function of the design parameter r on a log scale at fixed material coordinates $X = 3, 6, 12$.

Beginning with the rectangular lattice results, which are the bottom three graphs in Figure 3 and the left plot of Figure 5. The first key finding is a symmetry in the response about the the optimal design $r = 3.6$, which is the design that maximizes the initial spectral entropy decay, or 'slope' of the spectral entropy. This symmetry can be observed as the concave shape of the $h(r)$ curves in the left plot of Figure 5. The global minimum (mathematical optimization) of these curves occurs at the 'optimal' design at $r = 3.6$.

The Figure 3 graphs of $\Pi(X)$, $h(X)$ and $\Delta h(X)/\Delta X$ show the optimal design response (blue curve), which most resembles the continuum response (dashed curve). The symmetry in the $h(r)$ behavior about the optimal design in Figure 5 is expected to be reflected as symmetry in the responses in Figure 3 after changing the design parameter in either direction. Indeed, designs $r = 0.1$ (black curve) and $r = 100$ (pink curve) are nearly overlapping in their column energy, spectral entropy and spectral entropy decay responses. This overarching symmetry in the rectangular lattice is explained by the fact that the core dominated response $r << 1$ and reinforcement dominated response $r >> 1$ are the most anisotropic designs associated with the greatest degree of strain energy localization either by confinement along the midline or deflection along the angles of the rhombic reinforcement. This symmetry is broken in the triangular composite because of the rigid nature of the core (triangular) lattice.

Triangular lattice results are shown in the Figure 4 bottom graphs and the right plot of Figure 5. The optimal design $r = 3.2$ is the global minimum in the $h(r)$ curves. However, curves are no longer symmetric about this optimal design. Instead, using a very rigid triangular lattice core $r << 1$ maintains lower magnitudes of spectral entropy and greater rates of entropy decay at its surface compared to using a comparably rigid rectangular core. The loss of symmetry is demonstrated in Figure 4 where the core dominated $r = 0.1$ response (black curve) is now distinct from the reinforcement dominated $r = 100$ response (pink curve). As expected, the optimal design (blue curve) exhibits the lowest levels of entropy and the fastest entropy decay rate at its surface compared to the other designs, and is the most continuum-like.

Looking at both types of lattices, the $\Pi(X)$ profiles of all continuum-like designs exhibit high amounts of energy absorbed at the surface that quickly dissipates with distance. In contrast, highly anisotropic designs show flatter column strain energy profiles where strain energy is less concentrated at the surface yet penetrates with larger magnitudes into the interior. Additionally, there is correlation between column energy and spectral entropy behavior in that an isotropic continuum-like design has high rates of decay of column energy and spectral entropy while an anisotropic design has has lower rates of decay of column energy and spectral entropy

Also, all lattices investigated in the numerical experiments exhibited similar asymptotic behavior of the spectral entropy decay $\Delta h(X)/\Delta X$. Figures 3 and 4 show that the spectral entropy decay curves tend to merge together by $X = 20$. While initial rates of entropy decay are different for the different designs, as one moves sufficiently far into the material interior, the slopes level out and appear to converge to each other. To reiterate, near to the surface load, both the magnitude of the entropy and its decay rate are distinct across different designs while far enough away from the surface only the magnitude of the entropy is distinct. Because large differences in spectral entropy decay behavior between isotropic continuum-like and highly anisotropic designs coincide with large differences in spatial strain energy behavior, and this is most pronounced at the surface of the applied load, this is one argument why using the decay rate (and not just its magnitude) is better suited for distinguishing exotic metamaterial phenomena.

5. Conclusion

In this paper, the strain energy distribution and spectral entropy behavior was investigated for the composite lattices of Figure 1 type. The entropy behavior was tailored depending on the anisotropy of the lattice, which was controlled by a single

design parameter. Isotropic continuum-like behavior was associated with enhanced entropy decay near the surface and strain energy dispersion whereas highly anisotropic behavior lead to slow entropy decay at the surface and strain energy localization. A surprising result was that given sufficient distance from the surface load, the asymptotic rate of entropy decay was similar in all lattice metamaterials including those with high anisotropy, and was similar to the way entropy decays in isotropic continuum materials. This implies in practice that any exotic properties of metamaterials determined by their modal selectivity are generally better pronounced in the vicinity of loads, and that they tend to diminish on the periphery of these interesting material systems.

Appendix A. Parseval theorem

The mechanical version of the Parseval theorem [25, 26] for discrete lattices states that strain energy in a column of the lattice Π_n is expressed either as a summation of volumetric strain energy over the spatial index m or as a summation of spectral energy over the wavenumbers q. Equivalence of the volumetric and spectral representations of the column energy is discussed below.

Strain energy in a column Π_n is computed at a fixed horizontal location n by the summation of volumetric (spatial) strain energies W_{nm} (4) over the vertical nodal index m

$$\Pi_n = \sum_m W_{nm} = \frac{1}{2}\sum_m \sum_{n'} \sum_{m'} \mathbf{d}^*_{n'm'} \mathbf{K}_{n-n'm-m'} \mathbf{d}_{n'm'} \tag{A.1}$$

Starting from (A.1) where the summation is performed over the spatial index m, the Parseval theorem asserts it is possible to redefine this expression for Π_n so that the summation is performed over the wavenumber q. The derivation is outlined below.

The Fourier image of the displacement vector is defined

$$\tilde{\mathbf{d}}_n(q) = \sum_m \mathbf{d}_{nm} e^{-iqm} \tag{A.2}$$

The displacement vector can be viewed as the inverse transform of its own Fourier image

$$\mathbf{d}_{nm} = \frac{1}{M}\sum_q \tilde{\mathbf{d}}_n(q) e^{iqm} \tag{A.3}$$

Likewise, the complex conjugate of the displacement vector $\mathbf{d}^*_{nm}$ is the inverse transform of the complex conjugate of the same Fourier image

$$\mathbf{d}^*_{nm} = \frac{1}{M}\sum_{q'} \tilde{\mathbf{d}}^*_n(q') e^{-iq'm} \tag{A.4}$$

The displacement vector (A.3) and its complex conjugate (A.4) written at (n', m') are substituted into (A.1), which takes the form upon rearranging

$$\Pi_n = \frac{1}{2}\frac{1}{M^2}\sum_q \sum_{q'} \sum_{n'} \sum_m e^{-iq'm} e^{iqm} \tilde{\mathbf{d}}^*_{n'}(q') \sum_{m'} \mathbf{K}_{n-n'm-m'} \tilde{\mathbf{d}}_{n'}(q) \tag{A.5}$$

At every other index m, the sum over m' yields the same term $\tilde{\mathbf{K}}_{n-n'}\tilde{\mathbf{d}}_{n'}(q)$, where

$$\tilde{\mathbf{K}}_{n-n'} = \sum_{m-m'} \mathbf{K}_{n-n'm-m'} \tag{A.6}$$

For the rectangular lattice of Figure 1d

$$\tilde{\mathbf{K}}_{-1} = \tilde{\mathbf{K}}_1 = -\frac{\tilde{\mathbf{K}}_0}{2} = \begin{bmatrix} \frac{5\sqrt{3}r}{4} & 0 \\ 0 & \frac{3\sqrt{3}r}{4} \end{bmatrix} \tag{A.7}$$

For the triangular lattice of Figure 1e

$$\tilde{\mathbf{K}}_{-1} = \tilde{\mathbf{K}}_1 = -\frac{\tilde{\mathbf{K}}_0}{2} = \begin{bmatrix} \frac{r}{6}(9+\sqrt{3}) & 0 \\ 0 & \frac{r}{2}(1+\sqrt{3}) \end{bmatrix} \tag{A.8}$$

Also, the Fourier mode orthogonality

$$\sum_m e^{-iq'm} e^{iqm} = M\delta_{qq'} \tag{A.9}$$

with the Kronecker delta $\delta_{qq'}$

$$\delta_{qq'} = \begin{cases} 1, & q = q' \\ 0, & q \neq q' \end{cases} \tag{A.10}$$

removes the sum over q' in (A.5). Thus, the strain energy in a column at nodal index n

$$\Pi_n = \frac{1}{M}\sum_q \frac{1}{2}\sum_{n'} \tilde{\mathbf{d}}^*_{n'}(q)\tilde{\mathbf{K}}_{n-n'}\tilde{\mathbf{d}}_{n'}(q) \tag{A.11}$$

The term after the first sum (over q) is the spectral distribution of the strain energy

$$\tilde{W}_n(q) = \frac{1}{2}\sum_{n'} \tilde{\mathbf{d}}^*_{n'}(q)\tilde{\mathbf{K}}_{n-n'}\tilde{\mathbf{d}}_{n'}(q) \tag{A.12}$$

$\tilde{W}_n(q)$ defines a fraction of strain energy contained in a given Fourier mode of deformation, and is determined at fixed columns n in the lattice.

A superposition of spectral energies $\tilde{W}_n(q)$ for all wavenumbers q and normalizing by the factor $1/M$ (A.11) is equal to the sum of all spatial energy terms W_{nm} for the periodic nodes m (A.1). The Parseval energy theorem is then written concisely

$$\Pi_n = \sum_m W_{nm} = \frac{1}{M}\sum_q \tilde{W}_n(q) \tag{A.13}$$

Appendix B. Modal interference

Figure B.6 is a qualitative illustration of the deflection of displacements which in turn causes the deflection of strain energy. When the discrete Fourier transform is applied to the displacement field over the vertical index m, the solution is decomposed into a set of Fourier harmonics or eigenmodes of deformation each with a wavenumber q and spatial wavelength $2\pi/q$. Eigenmodes are harmonic profiles of deformation for the column of nodes in a lattice. If the harmonics are phase shifted by their

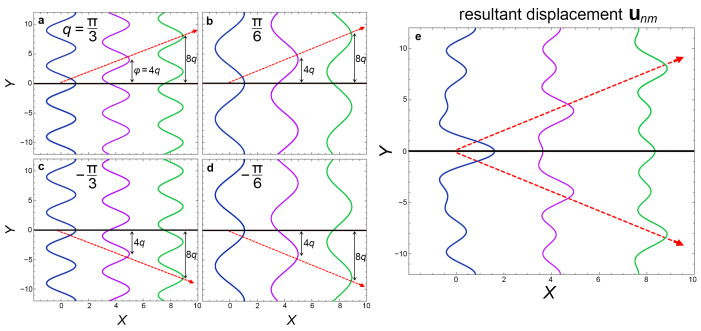

Figure B.6: Deflection of the displacement solution by modal interference. Material coordinates X and Y denote the horizontal and vertical position in the lattice, respectively. a)–d) Eigenmodes of deformation that are phase shifted by their wavenumber q at each subsequent lattice column located at X. The phase shift $\phi = Xq$. Eigenmodes at columns located at $X = 0$ (blue), 4 (purple) and 8 (green) are shown. Adding the positive and negative eigenmodes together results in an interference pattern that is shifted along angles (red arrows) when moving horizontally through the lattice. Positive wavelengths a) $\pi/3$ and b) $\pi/6$ are associated with upward deflection while negative wavelengths c) $-\pi/3$ and $-\pi/6$ are associated with downward deflection.

wavenumber at each subsequent column located at material coordinate X as in Figures B.6a–d then the resultant displacement solution $\mathbf{u}_{nm}$ shows an interference pattern with strong peaks that are shifted laterally as in Figure B.6e.

Mathematically, the components of the displacement solution $\mathbf{d}_{nm}$ for a lattice are proportional to sets of cosine terms each associated with an eigenmode with wavenumber q. For example, the horizontal displacements,

$$u_{nm} \propto \rho^n \cos(qm + \phi n) + \rho^n \cos(qm - \phi n) \qquad \text{(B.1)}$$

The displacement field is a function of the horizontal nodal index n, vertical index m, constant exponential factor ρ^n and phase angle ϕ. The first term on the right hand side corresponds to the positive wavenumber $+q$ Fourier harmonic, e.g., $q = \pi/3$ or $q = \pi/6$ in Figures B.6a–b, while the second term corresponds to the negative wavenumber $-q$ harmonic, e.g., $q = -\pi/3$ or $q = -\pi/6$ in Figures B.6c–d. Setting the phase angle ϕ equal to the wavenumber q of the eigenmode leads to an interference pattern resulting in the strain energy redirection due to (4). This represents an interesting analogy to the Bragg scattering of electromagnetic waves.

References

[1] M. Mirzaali, R. Hedayati, P. Vena, L. Vergani, M. Strano, A. Zadpoor, Rational design of soft mechanical metamaterials: Independent tailoring of elastic properties with randomness, Applied Physics Letters 111 (5) (2017) 051903.

[2] P. Ziemke, T. Frenzel, M. Wegener, P. Gumbsch, Tailoring the characteristic length scale of 3d chiral mechanical metamaterials, Extreme Mechanics Letters 32 (2019) 100553.

[3] Y. Wang, O. Sigmund, Quasiperiodic mechanical metamaterials with extreme isotropic stiffness, Extreme Mechanics Letters 34 (2020) 100596.

[4] T. A. Hewage, K. L. Alderson, A. Alderson, F. Scarpa, Double-negative mechanical metamaterials displaying simultaneous negative stiffness and negative poisson's ratio properties, Advanced Materials 28 (46) (2016) 10323–10332.

[5] H. M. Kolken, A. Zadpoor, Auxetic mechanical metamaterials, RSC advances 7 (9) (2017) 5111–5129.

[6] E. G. Karpov, L. A. Danso, J. T. Klein, Negative extensibility metamaterials: occurrence and design-space topology, Physical Review E 96 (2) (2017) 023002.

[7] J. Qu, M. Kadic, M. Wegener, Poroelastic metamaterials with negative effective static compressibility, Applied Physics Letters 110 (17) (2017) 171901.

[8] C. Yang, M. Boorugu, A. Dopp, J. Ren, R. Martin, D. Han, W. Choi, H. Lee, 4d printing reconfigurable, deployable and mechanically tunable metamaterials, Materials Horizons 6 (6) (2019) 1244–1250.

[9] Z. Wang, L. Jing, K. Yao, Y. Yang, B. Zheng, C. M. Soukoulis, H. Chen, Y. Liu, Origami-based reconfigurable metamaterials for tunable chirality, Advanced materials 29 (27) (2017) 1700412.

[10] E. G. Karpov, Structural metamaterials with saint-venant edge effect reversal, Acta Materialia 123 (2017) 245–254.

[11] H. Fang, S.-C. A. Chu, Y. Xia, K.-W. Wang, Programmable self-locking origami mechanical metamaterials, Advanced Materials 30 (15) (2018) 1706311.

[12] S. Janbaz, M. McGuinness, A. A. Zadpoor, Multimaterial control of instability in soft mechanical metamaterials, Physical Review Applied 9 (6) (2018) 064013.

[13] J. T. Klein, E. G. Karpov, Bistability in thermomechanical metamaterials structured as three-dimensional composite tetrahedra, Extreme Mechanics Letters 29 (2019) 100459.

[14] H. Yasuda, L. Korpas, J. Raney, Transition waves and formation of domain walls in multistable mechanical metamaterials, Physical Review Applied 13 (5) (2020) 054067.

[15] C. Coulais, D. Sounas, A. Alù, Static non-reciprocity in mechanical metamaterials, Nature 542 (7642) (2017) 461–464.

[16] M. Shaat, Nonreciprocal elasticity and the realization of static and dynamic nonreciprocity, Scientific Reports 10 (1) (2020) 1–13.

[17] E. Barchiesi, M. Spagnuolo, L. Placidi, Mechanical metamaterials: a state of the art, Mathematics and Mechanics of Solids 24 (1) (2019) 212–234.

[18] Biagil, Energy redistribution in damaged elastic frames, In print (2020).

[19] L. A. Danso, E. G. Karpov, Reprogramming static deformation patterns in mechanical metamaterials, Materials 11 (10) (2018) 2050.

[20] J. T. Klein, E. G. Karpov, Exact analytical solutions in two dimensional plate-like mechanical metamaterials: State of free deformation in a topological cylinder, International Journal of Mechanical Sciences 167 (2020) 105292.

[21] H. MI, K. R, Nonlinear bloch waves and balance between hardening and softening dispersion, Proceedings of the Royal Society A: Mathematical, Physical and Engineering Sciences 474 (2217) (2018) 20180173.

[22] M.-H. Lu, L. Feng, Y.-F. Chen, Phononic crystals and acoustic metamaterials, Materials today 12 (12) (2009) 34–42.

[23] E. Karpov, N. Stephen, D. Dorofeev, On static analysis of finite repetitive structures by discrete fourier transform, International Journal of Solids and Structures 39 (16) (2002) 4291–4310.

[24] B. Smith, D. Sandwell, Coulomb stress accumulation along the san andreas fault system, Journal of Geophysical Research: Solid Earth 108 (B6) (2003).

[25] E. G. Karpov, L. A. Danso, Strain energy spectral density and information content of materials deformation, International Journal of Mechanical Sciences 148 (2018) 676–683.

[26] E. G. Karpov, L. A. Danso, J. T. Klein, Anomalous strain energy transformation pathways in mechanical metamaterials, Proceedings of the Royal Society A 475 (2226) (2019) 20190041.

[27] C. E. Shannon, A mathematical theory of communication, The Bell system technical journal 27 (3) (1948) 379–423.

[28] V. Deshpande, M. Ashby, N. Fleck, Foam topology: bending versus stretching dominated architectures, Acta materialia 49 (6) (2001) 1035–1040.

[29] W. K. Liu, E. G. Karpov, H. S. Park, Nano mechanics and materials: theory, multiscale methods and applications, John Wiley & Sons, 2006.